Publication information

Title	Dirac cones at k$\rightarrow$ = 0 in phononic crystals
Author(s)	Liu, Fengming; Lai, Yun; Huang, Xueqin; Chan, C.T.
Source	Physical Review B , v. 84, (22), December 2011, Article number 224113
Version	Published version
DOI	https://doi.org/10.1103/PhysRevB.84.224113
Publisher	American Physical Society

Copyright information

Notice

http://repository.ust.hk/ir/

Dirac cones at $\vec{k}=0$ in phononic crystals

Fengming Liu,[1] Yun Lai,[1,2] Xueqin Huang,[1] and C. T. Chan[1,*]

[1]*Department of Physics, Hong Kong University of Science and Technology, Clear Water Bay, Hong Kong, China*
[2]*Department of Physics, Soochow University, China*

We show that two-dimensional phononic crystals exhibit Dirac cone dispersion at $\vec{k}=0$ by exploiting dipole and quadrupole accidental degeneracy. While the equifrequency surface of Dirac cone modes is almost isotropic, such systems exhibit super-anisotropy, meaning that only transverse waves are allowed along certain directions, while only longitudinal waves are allowed along some other directions. Only one mode, not two, is allowed near the Dirac point, and only two effective parameters, not four, are needed to describe the dispersion. Effective medium theory finds that the phononic crystals have effectively zero mass density and zero $1/C_{44}^{\mathrm{eff}}$ at the Dirac point. Numerical simulations are used to demonstrate the unusual elastic wave properties near the Dirac point frequency.

I. INTRODUCTION

Dirac points and Dirac cone dispersions can be found at the zone boundary of classical wave systems, such as photonic and acoustic wave crystals, and many interesting phenomena can be derived from these special dispersions.[1–9] Recently, it has been shown that Dirac cone dispersions can also be realized at $\vec{k}=0$[10] in some two-dimensional (2D) electromagnetic crystals comprising dielectric cylinders and that, in some cases, these crystals are related to a system with simultaneously zero permittivity and permeability through effective medium theory. This linkage has practical implication as it means that systems exhibiting zero permittivity and permeability[11–17] simultaneously can actually be implemented with pure dielectrics, without the need to use metallic resonators which have intrinsic loss.

It is well known that many intriguing characteristics of electromagnetic crystals can also be realized in acoustic and, in some cases, elastic crystals.[18–31] For acoustic waves in 2D, there exists a mapping between the acoustic wave problem and one polarization of the 2D electromagnetic wave problem. As such, we should be able to find Dirac cones at $\vec{k}=0$ for acoustic waves and map the acoustic crystal to a system with effectively zero mass density and zero reciprocal modulus. However, for elastic waves in a solid structure, the coexistence of longitudinal and transverse waves makes the problem much more complicated.

In this paper, we show new physics specific to elastic wave systems near the Dirac point at $\vec{k}=0$ by exploiting the accidental degeneracy. We will see that near the elastic wave Dirac point at $\vec{k}=0$, the equifrequency contours are nearly circles in contrast to ordinary 2D phononic crystals (PCs) with a square array (C_{4v} symmetry) whose dispersion is anisotropic even in the low-frequency regime.[32,33] On the other hand, the Dirac cone modes exhibit the so-called super-anisotropic behavior[34] as the k vector sweeps around the Brillouin zone such that only purely transverse waves are allowed along certain directions, while only longitudinal waves are allowed along some other directions. This behavior was recently found in a special kind of elastic wave metamaterial that has four components (steel, foam, and soft and hard rubber) with fairly complex resonating building blocks.[34] Here, we show

that super-anisotropy can arise naturally near the Dirac point in the simplest two-component PCs. In addition, effective medium theory found that PCs with a Dirac cone at $\vec{k}=0$ have effectively zero $1/C_{44}^{\mathrm{eff}}$ and zero mass density ρ_{eff}, and two effective parameters (instead of four) are sufficient to describe the dispersion. The elastic constants $C_{11}^{\mathrm{eff}}, C_{12}^{\mathrm{eff}}$ drop out of the description as $C_{11}^{\mathrm{eff}} \approx -C_{12}^{\mathrm{eff}}$ due to the dominance of quadrupolar mode near the Dirac point. The super-anisotropic behavior and the effective index of almost zero near the Dirac point frequencies are demonstrated using numerical simulations. These novel properties can neither be found in electromagnetic or acoustic wave systems nor in ordinary elastic wave materials.

II. METHODOLOGY

A. Physical system

The 2D PCs considered in this study are composed of rubber cylinders arranged in a square lattice in the xy plane embedded in an epoxy host. The lattice constant is denoted by a, and the radius of the cylinders is set to $R = 0.266a$. Both rubber and epoxy are taken to be isotropic, with the density ρ of rubber and epoxy taken to be 1.3×10^3 kg/m^3 and 1.18×10^3 kg/m^3, respectively. The velocity of longitudinal waves is $v_l = 817$ m/s ($v_{l0} = 2605$ m/s) and the velocity of transverse waves is $v_t = 335$ m/s ($v_{t0} = 1068$ m/s) in rubber (epoxy).

B. Describing the system using Christoffel's equation

From the theory of linear elasticity,[35,36] a two-dimensional square lattice elastic solid has three independent elastic moduli C_{11}, C_{12}, and C_{44}. The constitutive relation takes the form as

$$\begin{pmatrix} T_{xx} \\ T_{yy} \\ T_{xy} \end{pmatrix} = \begin{pmatrix} c_{11} & c_{12} & 0 \\ c_{12} & c_{11} & 0 \\ 0 & 0 & c_{44} \end{pmatrix} \begin{pmatrix} S_{xx} \\ S_{yy} \\ 2S_{xy} \end{pmatrix}, \qquad (1)$$

where T_{ij} is the stress tensor and $S_{ij} = \frac{1}{2}(\frac{\partial u_i}{\partial x_j} + \frac{\partial u_j}{\partial x_i})$ is the strain tensor and u_i is the displacement in the ith direction. By substituting Eq. (1) into Newton's second law, i.e. $\rho \partial^2 u_i / \partial t^2 = \partial T_{ij}/\partial x_j$ where ρ is mass density, and using a plane-wave solution of the form $u_i = u_i^0 F[t - (\mathbf{nx})/v]$, where

v is phase velocity, u_i^0 is the wave polarization giving the direction of the particle displacement, and n_i denotes the propagation direction, we get,

$$\rho v^2 u_i^0 = \Gamma_{il} u_l^0, \quad (2)$$

where $\Gamma_{il} = c_{ijkl} \mathrm{n}_j \mathrm{n}_k$ is the Christoffel tensor. In a two-dimensional square lattice elastic solid, Γ_{il} has the form

$$\Gamma_{il} = \begin{vmatrix} \Gamma_{11} & \Gamma_{12} \\ \Gamma_{12} & \Gamma_{22} \end{vmatrix}, \quad (3)$$

where $\Gamma_{11} = c_{11} \cos^2 \varphi + c_{44} \sin^2 \varphi$, $\Gamma_{22} = c_{11} \sin^2 \varphi + c_{44} \cos^2 \varphi$, and $\Gamma_{12} = (c_{12} + c_{44}) \sin \varphi \cos \varphi$. Here, φ denotes angle between the propagation direction and the x axis. By solving the Christoffel's equation of Eq. (2), we obtain two eigenvalues $\gamma_m = \rho v_m^2 (m = 1,2)$ as functions of the angle φ,

$$2\rho v_1^2 = C_{11} + C_{44}$$
$$+ \sqrt{(C_{11} - C_{44})^2 \cos^2 2\varphi + (C_{12} + C_{44})^2 \sin^2 2\varphi},$$
$$2\rho v_2^2 = C_{11} + C_{44}$$
$$- \sqrt{(C_{11} - C_{44})^2 \cos^2 2\varphi + (C_{12} + C_{44})^2 \sin^2 2\varphi}.$$
$$(4)$$

For each eigenvalue $\gamma_m (m = 1,2)$ there is a corresponding eigenvector u_{mi}^0 whose components satisfy Eq. (2)

$$(\Gamma_{11} - \gamma_m) u_{mx}^0 + \Gamma_{12} u_{my}^0 = 0,$$
$$\Gamma_{12} u_{mx}^0 + (\Gamma_{22} - \gamma_m) u_{my}^0 = 0. \quad (5)$$

The polarizations of the plane waves, defined by the angles which β_m makes with the x axis, can be obtained from the equation $\tan \beta_m = \frac{u_{my}^0}{u_{mx}^0}$. In general, the polarizations of the plane waves with phase velocities v_1 and v_2 are neither transverse nor longitudinal except in the high-symmetry directions (e.g. ΓX and ΓM directions).

III. RESULTS AND DISCUSSION

A. Band structure

Figure 1(a) shows the band structure of our system that exhibits a Dirac point at $\vec{k} = 0$. The dispersions are calculated using a numerical solver (COMSOL Multiphysics) for the in-plane (xy) modes,[37,38] which include the longitudinal and transverse vibrations in the plane perpendicular to the cylinder's axis. As shown in the enlarged view of the band structure, two cones are formed by the linear branches and touches at a Dirac point at $\vec{k} = 0$ [with frequency $\omega_0 = 0.721(2\pi v_{t0}/a)$]. A flat branch with a small group velocity also intersects at the Dirac point. This flat band can be interpreted as a consequence of the zero effective density of the system.[19] If the zero-effective-density system is perfectly homogeneous, the band will be dispersionless, and thus the band will be a deaf band which does not couple with external waves. But in any real PC, which comprises discrete building blocks, there is always some spatial dispersion so that the band is not perfectly dispersionless away from the zone center, and the flat band can be excited if external wave is incident with nonzero k-parallel components.

To illustrate the Dirac cones visually, the three-dimensional dispersion surfaces near the Dirac point frequency are plotted in Fig. 1(b). Figure 1(c) shows the equifrequency surface at
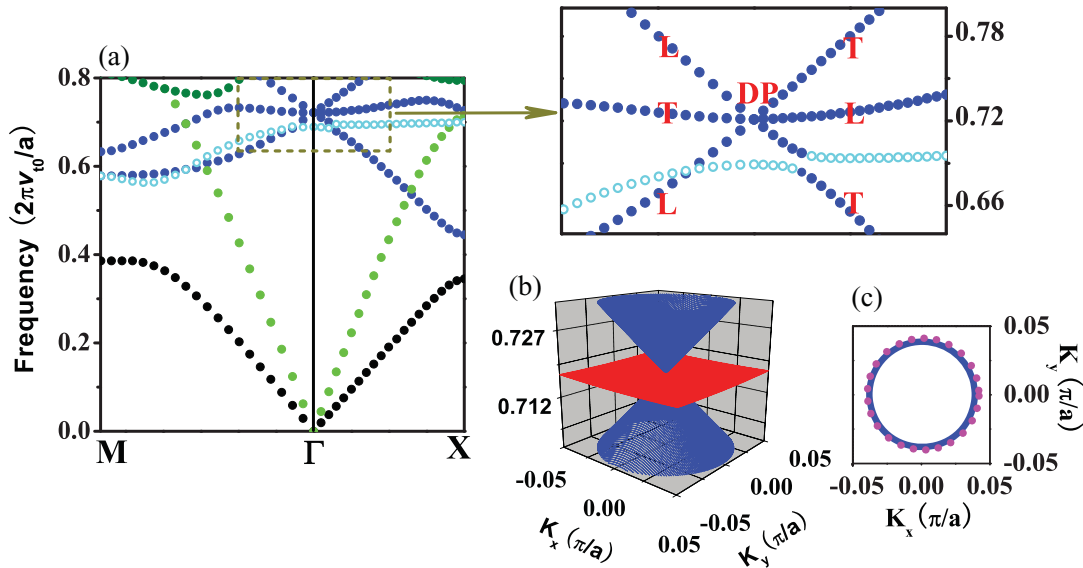

FIG. 1. (Color online) (a) Band structure for the in-plane modes. The inset provides an enlarged view of the band dispersion near the Dirac point. Two linear bands intersect at a Dirac point, $\omega = 0.721(2\pi v_{t0}/a)$, and a third band with small group velocity also crosses that point. Here, v_{t0} is the transverse wave velocity of epoxy; T and L denote transverse and longitudinal modes, respectively, and DP denotes Dirac point. (b) Three-dimensional dispersion surfaces near the Dirac point frequency showing the relationship between the frequency and wave vector. The linear bands (blue/medium gray) form cones that touch at the Dirac point. There is an additional sheet (red/dark gray) corresponding to the flat band that can be interpreted as additional solutions due to a zero effective density [see text and part (F) in supplementary material]. (c) The equifrequency surfaces of the PCs calculated numerically (blue/medium gray circle) and those derived from the boundary effective medium theory (magenta/light gray dot) at frequency [$\omega = 0.712(2\pi v_{t0}/a)$] below the Dirac point. Note that the equifrequency is essentially circular and is described well by the effective medium parameters shown in Fig. 3.

a frequency that is slightly below the Dirac point. We note in particular that the equifrequency contour is circular. This is not required by symmetry in a cubic-elastic-wave system in which the equifrequency contours (or equivalently, the slowness surfaces) are anisotropic, even in the low frequency limit.[33] This emerges as a special property of a Dirac cone which in turn is derived from the accidental degeneracy of the dipolar and quadrupolar degrees of freedom.

B. Multiple scattering theory analysis

We apply multiple scattering theory (MST) to obtain the condition of the accidental degeneracy. The dispersion relations of a phononic crystal are determined by the solutions to the following secular equation:

$$\det \left| \begin{pmatrix} T^{ll}G^l & T^{lt}G^t \\ T^{tl}G^l & T^{tt}G^t \end{pmatrix} - I \right| = 0, \tag{6}$$

where $T^{\alpha,\beta}$ is the T matrix with matrix elements $t_{mm'}^{\alpha\beta} = D_m^{\alpha\beta}\delta_{mm'}$ and $D_m^{\alpha\beta}$ is the elastic Mie scattering coefficient of angular momentum number m for the scatter. Here, α and β can take the values of l and t, which denote, respectively, the longitudinal and transverse waves. Explicit expressions of the elastic Mie scattering coefficient $D_m^{\alpha\beta}$ can be found in the literature.[23] Here, G^l and G^t denote the matrices with matrix elements given by the lattice sum $G_{m'm}^{\beta} = \sum_{q\neq p} g_{m'm''}^{\beta} e^{i\vec{K}\vec{R}_q} (\beta = l,t)$,

and the lattice sum is given by

$$\sum_{q\neq p} g_{m'm''}^{\beta} e^{i\vec{K}\vec{R}_q} = S(\beta, m' - m''), \tag{7}$$

where

$$S(\beta,n) = \frac{1}{J_{n+1}(k_{\beta0}a)} \left\{ \frac{4i^{n+1}k_{\beta0}}{\Omega} \sum_h \frac{J_{n+1}(Q_h a)}{Q_h(k_{\beta0}^2 - Q_h^2)} e^{-in\phi_h} \right.$$
$$\left. - \left[H_1^{(1)}(k_{\beta0}a) + \frac{2i}{\pi k_{\beta0}a} \right] \delta_{n,0} \right\}_{(n\geqslant0)}, \tag{8}$$

$$S(\beta,-n) = -S^*(\beta,n).$$

Here, $\vec{Q}_h = (Q_h,\phi_h)$ denotes the vector $\vec{K} + \vec{K}_h$, where $\vec{K} = (K,\phi_K)$ and $\vec{K}_h = (K_h,\phi_{Kh})$ represent, respectively, the Block wave vector and reciprocal-lattice vector. Here, $k_{l0} = \omega\sqrt{(\kappa_0 + \mu_0)/\rho_0}$ and $k_{t0} = \omega\sqrt{\mu_0/\rho_0}$ are the wave vectors inside the host, where κ_0, μ_0, and ρ_0 are the material parameters of the host. Here, $J_{n+1}(x)$ and $H_1^{(1)}(x)$ are the Bessel and Hankel functions, respectively. From the eigenstate fields near the Dirac point, we know they are mainly dipolar ($m = \pm1$) and quadrupolar ($m = \pm2$) modes. We can hence apply the MST to the subspace spanned by dipolar and quadrupolar modes. At $\vec{k} = 0$ for the square lattice, the lattice symmetry requires that $S(\beta,0) \neq 0$, $S(\beta,\pm1) = S(\beta,\pm2) = S(\beta,\pm3) = 0$, and $S(\beta,\pm4) \neq 0$.[33] Thus, the secular equation can be simplified as

$$\begin{vmatrix} D_2^{ll}S(l,0)-1 & 0 & 0 & D_2^{ll}S(l,4) & D_2^{lt}S(t,0) & 0 & 0 & D_2^{lt}S(t,4) \\ 0 & D_1^{ll}S(l,0)-1 & 0 & 0 & 0 & D_1^{lt}S(t,0) & 0 & 0 \\ 0 & 0 & D_{-1}^{ll}S(l,0)-1 & 0 & 0 & 0 & D_{-1}^{lt}S(t,0) & 0 \\ D_{-2}^{ll}S(l,-4) & 0 & 0 & D_{-2}^{ll}S(l,0)-1 & D_{-2}^{ll}S(t,-4) & 0 & 0 & D_{-2}^{lt}S(t,0) \\ D_2^{tl}S(l,0) & 0 & 0 & D_2^{tl}S(l,4) & D_2^{tt}S(t,0)-1 & 0 & 0 & D_2^{tt}S(t,4) \\ 0 & D_1^{tl}S(l,0) & 0 & 0 & 0 & D_1^{tt}S(t,0)-1 & 0 & 0 \\ 0 & 0 & D_{-1}^{tl}S(l,0) & 0 & 0 & 0 & D_{-1}^{tt}S(t,0)-1 & 0 \\ D_{-2}^{tl}S(l,-4) & 0 & 0 & D_{-2}^{tl}S(l,0) & D_{-2}^{tt}S(t,-4) & 0 & 0 & D_{-2}^{tt}S(t,0)-1 \end{vmatrix} = 0. \tag{9}$$

Equation (9) can be transformed to

$$\begin{vmatrix} D_2^{ll}S(l,0)-1 & D_2^{lt}S(t,0) & D_2^{lt}S(t,4) & D_2^{ll}S(l,4) & 0 & 0 & 0 & 0 \\ D_2^{tl}S(l,0) & D_2^{tt}S(t,0)-1 & D_2^{tt}S(t,4) & D_2^{tl}S(l,4) & 0 & 0 & 0 & 0 \\ D_{-2}^{tl}S(l,-4) & D_{-2}^{tt}S(t,-4) & D_{-2}^{tt}S(t,0)-1 & D_{-2}^{tl}S(l,0) & 0 & 0 & 0 & 0 \\ D_{-2}^{ll}S(l,-4) & D_{-2}^{lt}S(t,-4) & D_{-2}^{lt}S(t,0) & D_{-2}^{ll}S(l,0)-1 & 0 & 0 & 0 & 0 \\ 0 & 0 & 0 & 0 & D_1^{ll}S(l,0)-1 & D_1^{lt}S(t,0) & 0 & 0 \\ 0 & 0 & 0 & 0 & D_1^{tl}S(l,0) & D_1^{tt}S(t,0)-1 & 0 & 0 \\ 0 & 0 & 0 & 0 & 0 & 0 & D_{-1}^{ll}S(l,0)-1 & D_{-1}^{lt}S(t,0) \\ 0 & 0 & 0 & 0 & 0 & 0 & D_{-1}^{tl}S(l,0) & D_{-1}^{tt}S(t,0)-1 \end{vmatrix} = 0. \tag{10}$$

As the cylindrical symmetry of the cylinders ensures that $D_1^{ll} = D_{-1}^{ll}, D_1^{tt} = D_{-1}^{tt}, D_1^{lt} = D_{-1}^{lt}$ and $D_1^{tl} = D_{-1}^{tl}$, we have

$$\begin{vmatrix} D_1^{ll}S(l,0)-1 & D_1^{lt}S(t,0) \\ D_1^{tl}S(l,0) & D_1^{tt}S(t,0)-1 \end{vmatrix} = \begin{vmatrix} D_{-1}^{ll}S(l,0)-1 & D_{-1}^{lt}S(t,0) \\ D_{-1}^{tl}S(l,0) & D_{-1}^{tt}S(t,0)-1 \end{vmatrix} = 0, \tag{11}$$

which yields doubly degenerate orthogonal dipolar eigenmodes at a particular frequency ω_d. As the lattice sum $S(\beta, \pm 4) \neq 0$, the quadrupolar modes interact with each other and split into two nondegenerate modes. Thus,

$$
\begin{vmatrix}
D_2^{ll} S(l,0) - 1 & D_2^{lt} S(t,0) & D_2^{lt} S(t,4) & D_2^{ll} S(l,4) \\
D_2^{tl} S(l,0) & D_2^{tt} S(t,0) - 1 & D_2^{tt} S(t,4) & D_2^{tl} S(l,4) \\
D_{-2}^{tl} S(l,-4) & D_{-2}^{tt} S(t,-4) & D_{-2}^{tt} S(t,0) - 1 & D_{-2}^{tl} S(l,0) \\
D_{-2}^{ll} S(l,-4) & D_{-2}^{lt} S(t,-4) & D_{-2}^{lt} S(t,0) & D_{-2}^{ll} S(l,0) - 1
\end{vmatrix} = 0,
\tag{12}
$$

which yields two nondegenerate quadrupolar solutions at $\vec{k} = 0$. We shall label these two frequencies as $\omega_{q(2)}$ and $\omega_{q(-2)}$. The frequencies of these quadrupolar modes are not required by symmetry to be related to the dipolar modes, but if we tune the structural parameters such as the cylinder diameter, one of them can be equal to the dipolar mode solution $\omega_d = \omega_{q(2)}$ [or $\omega_d = \omega_{q(-2)}$]. This is type of degeneracy is called accidental degeneracy as it is not required by the symmetry of the system, and we can realize accidental degeneracy for our elastic wave system simply by tuning structural parameters.

C. The displacement fields near the Dirac point

Figure 2 shows the displacement field distributions of the eigenstates near the Dirac point with a small $\vec{k}$ along the ΓX direction ($k_x = 0.01 \times \pi/a$, $k_y = 0.0 \times \pi/a$) and the ΓM direction ($k_x = 0.01 \times \pi/a$, $k_y = 0.01 \times \pi/a$). In Figs. 2(a) and 2(b), we show the imaginary and real parts of the displacement fields of the lowest frequency state [$\omega = 0.720(2\pi v_{t0}/a)$]. The eigenmode of this linear band which forms the Dirac cone is a linear combination of quadrupole and dipole excitations. Figure 2(b) shows that the dipole displacement is perpendicular to k, and the quadrupolar mode couples only to transversely polarized incident waves, and thus the linear band is a band of transverse modes along ΓX direction. The eigenmode for the highest frequency state [$\omega = 0.722(2\pi v_{t0}/a)$] (not shown here), which belongs to the upper Dirac cone, is also a linear combination of a quadrupole and a transverse dipole. The real part of the eigenmode of the flat band, which has a frequency sandwiched between the upper and lower Dirac cones, is plotted in Fig. 2(c), and the imaginary part is almost zero. We can see that it is a pure dipolar mode
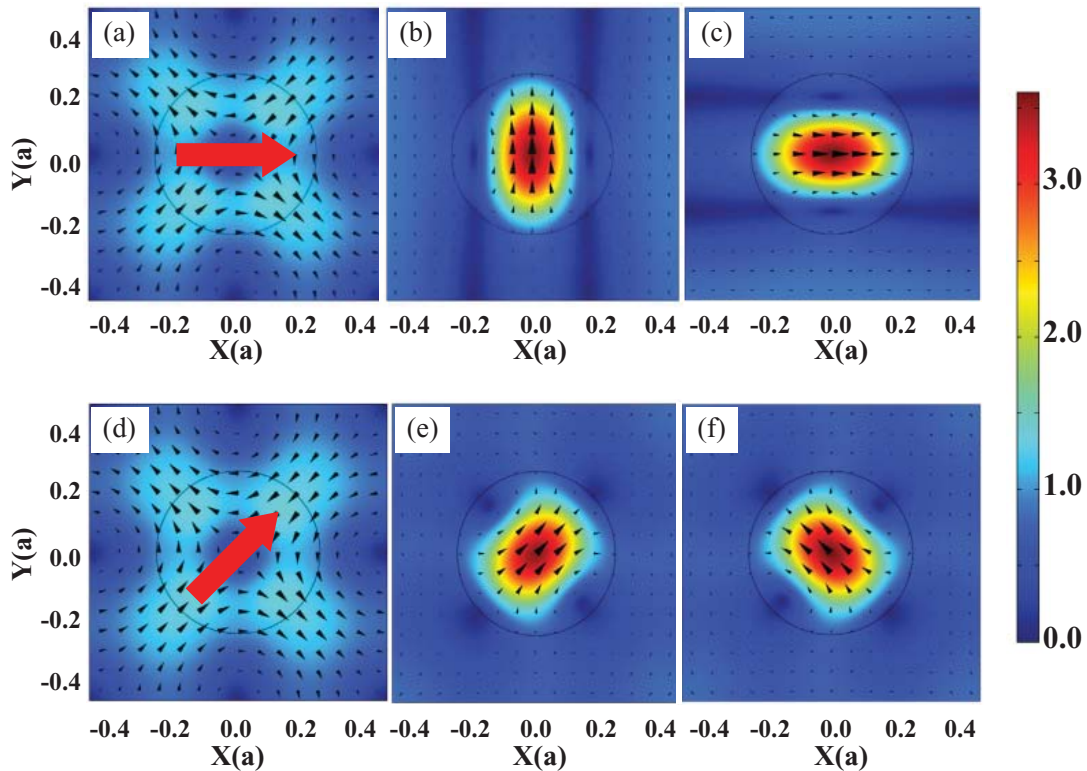

FIG. 2. (Color online) (a)–(c) The displacement field distributions of the eigenstates near the Dirac point with a small $\vec{k}$ along the ΓX direction: (a) the imaginary part and (b) the real part of the displacement fields of the linear band at frequency $\omega = 0.720(2\pi v_{t0}/a)$; (c) the real part of the displacement fields of the flat band at frequency $\omega = 0.721(2\pi v_{t0}/a)$. (d)–(f) The displacement field distributions of the eigenstates near the Dirac point with a small $\vec{k}$ along the ΓM direction: (d) the imaginary part and (e) the real part of the displacement fields of the linear band at frequency $\omega = 0.720(2\pi v_{t0}/a)$; (f) the real part of the displacement fields of the flat band at frequency $\omega = 0.721(2\pi v_{t0}/a)$. The black arrows denote the directions of the displacement, and the red/dark gray arrows in panels (a) and (d) indicate the direction of wave vector $\vec{k}$.

polarized parallel to the wave vector $\vec{k}$. Thus, the flat band is a longitudinal wave band near the Dirac point in the ΓX direction.

By contrast, the nature of waves is different in the ΓM direction. Figures 2(d) and 2(e) show the imaginary and real parts of the displacement fields of the lowest frequency state $[\omega = 0.720(2\pi v_{t0}/a)]$, which belongs to the lower Dirac cone. The polarization of the eigenmode is completely changed along ΓM. While the eigenmode along ΓM is also a combination of a quadrupole and a dipole, the dipolar mode is along the wave vector direction, while the quadrupolar mode can only be excited by longitudinal waves. Therefore, the linear band is a pure longitudinal wave band in the ΓM direction. The eigenmode for the highest frequency state $[\omega = 0.722(2\pi v_{t0}/a)]$ (not shown here), which belongs to the upper Dirac cone, is also similar to that for the lowest frequency state. The real part of the eigenmode of the flat band is plotted in Fig. 2(f). As it is a pure dipolar mode perpendicular to the wave vector $\vec{k}$, the nature of the flat band is also different. Figures 1(b) and 1(c) show that the Dirac cone modes have isotropic dispersion (circular equifrequency contours), but Fig. 2 shows that the Dirac cone modes are super-anisotropic, as they are purely transverse in one direction but purely longitudinal in another.

Located below the Dirac point [at about $\sim 0.7(2\pi v_{t0}/a)$], the branch marked by cyan/gray open circles corresponds to a rotation mode confined inside the rubber cylinder. This mode is highly confined and nearly dispersionless along ΓX. Due to the hybridization with this rotation mode, the mode pattern of the linear branch near the avoided crossing point along ΓX [$\sim 0.7(2\pi v_{t0}/a)$] is rather complex and cannot be taken as simple mixtures of quadrupolar and dipolar excitations.

D. Effective medium description

We note that the energy associated with displacement fields of the eigenstates near the Dirac point mainly localize in the rubber cylinders as the wave velocity of rubber is lower than the wave velocity of epoxy, and the displacement fields are fairly homogeneous in the matrix composite. It has been argued[39,40] that, near the standing wave frequency, homogenization theory is still valid near $\vec{k} = 0$ for periodic media, even if the frequency is relatively high. Here, we employed the boundary-effective medium theory[34] to obtain the effective parameters for the Dirac cone modes of our structure, even though the Dirac point has a relatively high frequency. We remark here that the effective medium description can be made as accurate as we like by lowering the Dirac point frequency, which can in principle be achieved if we employ a softer material for the cylinder inclusions. In this study, however, we stuck with commonly available materials. The use of the effective medium description is justified since our numerical simulations showed that the effective parameters can indeed predict the wave transmission properties reasonably well. It is known that dipolar and quadrupolar resonances are associated with mass density and certain components of elastic moduli, respectively.[22,23] We will see that the transport properties of our system can be understood if we can obtain the effective medium parameters.
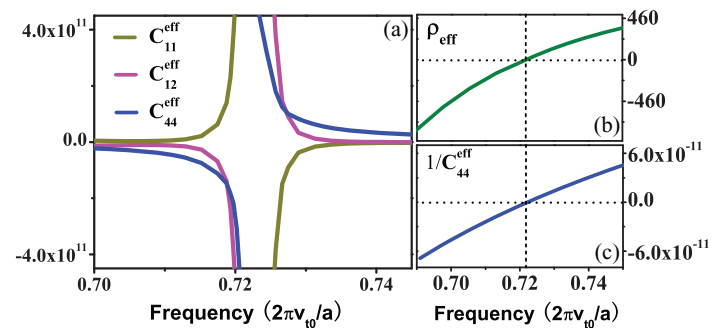

FIG. 3. (Color online) (a) The effective moduli C_{11}^{eff}, C_{12}^{eff}, and C_{44}^{eff}; (b) the effective mass density ρ_{eff}; and (c) the reciprocal of effective modulus, $1/C_{44}^{\text{eff}}$, of the PC as a function of frequency near the Dirac point.

We show the effective moduli C_{11}^{eff}, C_{12}^{eff}, and C_{44}^{eff} of the PC as functions of frequency in Fig. 3(a). For most known materials, the elastic moduli C_{11} and C_{12} are both positive, and the strains S_{xx} and S_{yy} compress or extend simultaneously under external stress. However, the quadrupolar mode displacement corresponds to compression in one direction and simultaneous extension in the orthogonal direction, and thus C_{11}^{eff} and C_{12}^{eff} have opposite signs here if the field displacements have a quadrupolar mode pattern. It can be seen from Fig. 3(a) that C_{11}^{eff} and C_{12}^{eff} actually have opposite signs and $C_{11}^{\text{eff}} \approx -C_{12}^{\text{eff}}$. In addition, all the effective moduli C_{11}^{eff}, C_{12}^{eff}, and C_{44}^{eff} evaluated using the eigenmode appear to diverge near the Dirac point due to the quadrupolar resonance. In Fig. 3(b), the effective mass density ρ_{eff} of the PC as a function of frequency is plotted. It can be seen that ρ_{eff} approaches zero at the Dirac point frequency. The PC generally allows for two in-plane modes whose phase velocities v_1 and v_2 can be obtained using the Christoffel's equations and the effective elastic parameters found above.

Below the Dirac point frequency, we find that $C_{11}^{\text{eff}} > 0$, $C_{44}^{\text{eff}} < 0$, and in particular $C_{12}^{\text{eff}} \approx -C_{11}^{\text{eff}}$ due to quadrupolar resonance. The eigenvalues γ_1 and γ_2 [Eq. (4)] reduce to $\gamma_1 = \rho_{\text{eff}} v_1^2 = C_{11}^{\text{eff}}$ and $\gamma_2 = \rho_{\text{eff}} v_2^2 = C_{44}^{\text{eff}}$, respectively, for any propagation direction φ. For $\rho_{\text{eff}} < 0$, $v_1 = \sqrt{C_{11}^{\text{eff}}/\rho_{\text{eff}}}$ is imaginary and $v_2 = \sqrt{C_{44}^{\text{eff}}/\rho_{\text{eff}}}$ is real. Thus, only the branch with eigenvalue γ_2 is allowed for the lower band. With the eigenvalue γ_2, we can also obtain the polarization of the plane wave in the high-symmetry directions by using Eq. (5). For the ΓX direction $\varphi = 0°$, $\Gamma_{11} = c_{11}^{\text{eff}}$, $\Gamma_{22} = c_{44}^{\text{eff}}$, and $\Gamma_{12} = 0$. Thus, Eq. (5) becomes

$$\left(c_{11}^{\text{eff}} - c_{44}^{\text{eff}}\right)u_{2x}^0 = 0, \quad \left(c_{44}^{\text{eff}} - c_{44}^{\text{eff}}\right)u_{2y}^0 = 0. \quad (13)$$

It can be seen that $u_{2x}^0 = 0$ and u_{2y}^0 are arbitrary. Thus, $\tan \beta_{2(\Gamma X)} = \frac{u_{2y}^0}{u_{2x}^0} = \infty$, and $\beta_{2(\Gamma X)} = 90°$, which indicates that the plane wave is a transverse wave in the ΓX direction. For the ΓM direction $\varphi = 45°$, $\Gamma_{11} = \frac{(c_{11}^{\text{eff}} + c_{44}^{\text{eff}})}{2}$, $\Gamma_{22} = \frac{(c_{11}^{\text{eff}} + c_{44}^{\text{eff}})}{2}$, and $\Gamma_{12} = \frac{(c_{44}^{\text{eff}} - c_{11}^{\text{eff}})}{2}$. Thus, Eq. (5) becomes

$$\frac{\left(c_{11}^{\text{eff}} - c_{44}^{\text{eff}}\right)}{2}u_{2x}^0 + \frac{\left(c_{44}^{\text{eff}} - c_{11}^{\text{eff}}\right)}{2}u_{2y}^0 = 0,$$

$$\frac{\left(c_{44}^{\text{eff}} - c_{11}^{\text{eff}}\right)}{2}u_{2x}^0 + \frac{\left(c_{11}^{\text{eff}} - c_{44}^{\text{eff}}\right)}{2}u_{2y}^0 = 0. \quad (14)$$

Thus, it can be seen that $\tan \beta_{2(\Gamma M)} = \frac{u_{2y}^0}{u_{2x}^0} = 1$, and $\beta_{2(\Gamma M)} = 45°$, which indicates that the plane wave is a longitudinal wave in the ΓM direction.

Above the Dirac point frequency, with $C_{11}^{\text{eff}} < 0$, $C_{44}^{\text{eff}} > 0$, and $C_{12}^{\text{eff}} \approx -C_{11}^{\text{eff}}$, the eigenvalues γ_1 and γ_2 [Eq. (4)] reduce to $\gamma_1 = \rho_{\text{eff}} v_1^2 = C_{44}^{\text{eff}}$ and $\gamma_2 = \rho_{\text{eff}} v_2^2 = C_{11}^{\text{eff}}$, respectively, for any propagation direction φ. For $\rho_{\text{eff}} > 0$, $v_1 = \sqrt{C_{44}^{\text{eff}}/\rho_{\text{eff}}}$ is real and $v_2 = \sqrt{C_{11}^{\text{eff}}/\rho_{\text{eff}}}$ is imaginary. Thus, this time, only the branch with eigenvalue γ_1 is allowed for the higher band. Again, with the eigenvalue γ_1, we can obtain the polarization of the plane wave in the high-symmetry directions by using Eq. (5). For the ΓX direction $\varphi = 0°$, $\Gamma_{11} = c_{11}^{\text{eff}}$, $\Gamma_{22} = c_{44}^{\text{eff}}$, and $\Gamma_{12} = 0$. Thus, Eq. (5) becomes

$$(c_{11}^{\text{eff}} - c_{44}^{\text{eff}})u_{1x}^0 = 0, \quad (c_{44}^{\text{eff}} - c_{44}^{\text{eff}})u_{1y}^0 = 0. \quad (15)$$

It can be seen that $u_{1x}^0 = 0$ and u_{1y}^0 are arbitrary. Thus, $\tan \beta_{1(\Gamma X)} = \frac{u_{1y}^0}{u_{1x}^0} = \infty$, and $\beta_{1(\Gamma X)} = 90°$, which indicates that the plane wave is a transverse wave in the ΓX direction. For the ΓM direction $\varphi = 45°$, $\Gamma_{11} = \frac{(c_{11}^{\text{eff}} + c_{44}^{\text{eff}})}{2}$, $\Gamma_{22} = \frac{(c_{11}^{\text{eff}} + c_{44}^{\text{eff}})}{2}$, and $\Gamma_{12} = \frac{(c_{44}^{\text{eff}} - c_{11}^{\text{eff}})}{2}$. Thus, Eq. (5) becomes

$$\frac{(c_{11}^{\text{eff}} - c_{44}^{\text{eff}})}{2}u_{1x}^0 + \frac{(c_{44}^{\text{eff}} - c_{11}^{\text{eff}})}{2}u_{1y}^0 = 0,$$
$$\frac{(c_{44}^{\text{eff}} - c_{11}^{\text{eff}})}{2}u_{1x}^0 + \frac{(c_{11}^{\text{eff}} - c_{44}^{\text{eff}})}{2}u_{1y}^0 = 0. \quad (16)$$

Thus, it can be seen that $\tan \beta_{1(\Gamma M)} = \frac{u_{1y}^0}{u_{1x}^0} = 1$, and $\beta_{1(\Gamma M)} = 45°$, which indicates that the plane wave is a longitudinal wave in the ΓM direction.

At the Dirac point frequency, both eigenvalues γ_1 and γ_2 are allowed simultaneously, thus super-anisotropy vanishes. Considering all these cases above, we can see that, near the Diarc point frequency, the velocities of the in-plane modes of the PCs only depend on the modulus C_{44}^{eff} for any propagation direction φ, and thus the equifrequency surface is circular. Furthermore, the super-anisotropy of the PC near the Dirac point frequency can be proved analytically using the effective medium parameters obtained.

In Fig. 3(c), the reciprocal of effective modulus, $1/C_{44}^{\text{eff}}$, is plotted as a function of frequency. It can be seen that $1/C_{44}^{\text{eff}}$ also approaches zero at the Dirac point frequency. The dispersion curves near the Dirac point of our system can be obtained using ρ_{eff} and C_{44}^{eff} and the relation $k = \omega \sqrt{\rho_{\text{eff}}/C_{44}^{\text{eff}}}$. The result is plotted in Fig. 1(c), where the result obtained using numerical methods is also shown. The good agreement between the numerically calculated (blue/medium gray circle) and the effective medium (magenta/light gray dot) results indicates that our effective medium theory is good near the Dirac point. Both ρ_{eff} and $1/C_{44}^{\text{eff}}$, which approach zero at the Dirac point frequency ω_0 simultaneously, are proportional to $\Delta\omega$. Since $k = \omega \sqrt{\rho_{\text{eff}}/C_{44}^{\text{eff}}}$, and ω can be considered constant as it is approximately equals ω_0, k is also proportional to $\Delta\omega$, which indicates that the dispersion curves are linear. The fact that the equifrequency contours of our system near the Dirac point are circular gives numerical support to the analysis above.

E. Transmission properties of the system

Figure 4 shows the results of numerical simulations which demonstrate the unusual wave propagation properties of the PC. Panels (a), (b), (f), and (g) illustrate the super-anisotropic properties. To avoid the influence of the flat band (as shown in Fig. 1), we set the working frequency to $\omega = 0.745(2\pi v_{t0}/a)$, slightly above the Dirac point frequency. For incidence along the ΓX direction, panel (a) shows that transverse waves can pass through the PC slab, while panel (b) shows that longitudinal waves are rejected. In the ΓM incidence direction, panel (f) shows that transverse waves are rejected, while panel (g) shows that longitudinal waves can pass through the slab.
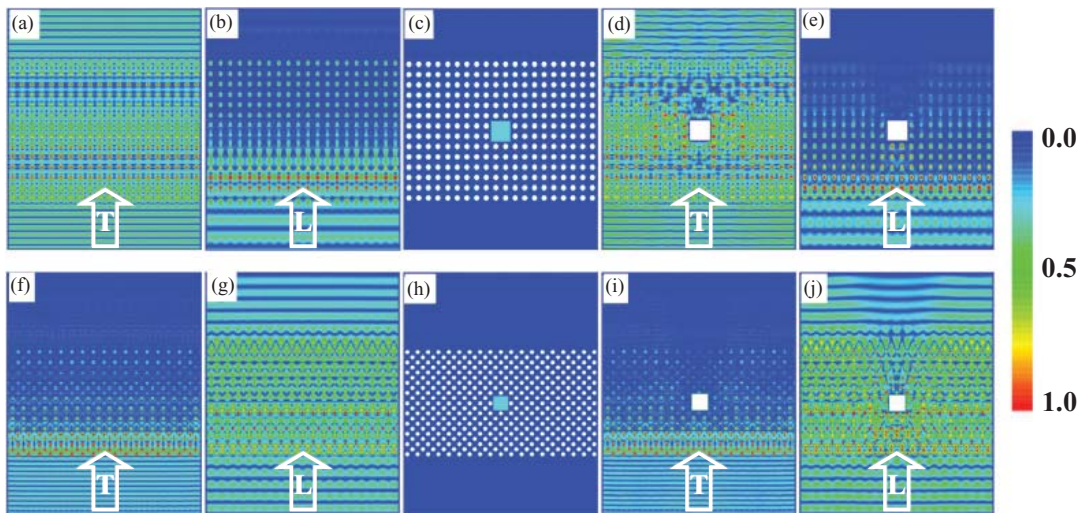

FIG. 4. (Color online) In the ΓX incidence direction: panel (a) shows that transverse waves can pass through the PC slab, while panel (b) shows that longitudinal waves are rejected; (c) the geometry of a steel object embedded in the epoxy host surrounded by the PC; panel (d) shows that transverse waves can go around an obstacle, while panel (e) shows that longitudinal waves are again rejected. In the ΓM incidence direction: (h) the geometry of a steel object embedded in the epoxy host surrounded by the PC; (f), (g), (i), and (j) show that in the ΓM direction, longitudinal waves can pass through, but transverse waves are rejected. The working frequency is $\omega = 0.745(2\pi v_{t0}/a)$, slightly above the Dirac point; T and L denote transverse and longitudinal incident waves, respectively.
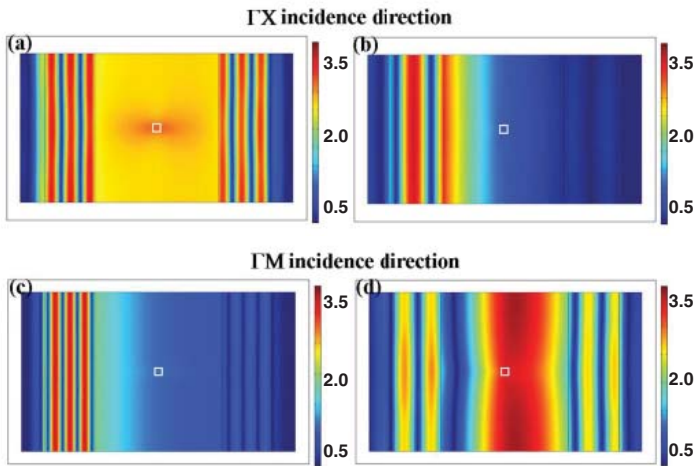
FIG. 5. (Color online) The numerically simulated displacement field distributions for a homogeneous anisotropic medium with the effective medium parameters (ρ_{eff}, C_{11}^{eff}, C_{12}^{eff}, and C_{44}^{eff}) at the frequency above the Dirac point frequency. Panel (a) shows that, in the ΓX direction, transverse waves can pass through the homogeneous medium, even going around an obstacle, but panel (b) shows that longitudinal waves are rejected. (c) and (d) show that, in the ΓM direction, longitudinal waves can pass, and transverse waves are rejected. For all the cases, plane waves are incident from the left.

Since ρ_{eff} and $1/C_{44}^{\text{eff}}$ go through zero simultaneously and linearly as the frequency passes through the Dirac point, the effective refractive index approaches zero, but the group velocity remains finite at the Dirac point. So, the PC should have the interesting wave propagation characteristics of a zero-index material.

Figure 4(c) [Fig. 4(h)] shows the schematic of a structure with a steel object embedded in the epoxy host and surrounded by the PC for the ΓX (ΓM) incidence direction. In Fig. 4(d), a transverse plane-wave impinges on the structure (ΓX incidence), and the displacement field distributions show that the incidence wave can pass through the PC, and the wave is not obstructed by the steel obstacle. The transverse wave is able to pass through, preserving its plane-wave characteristic in the presence of the steel object. If the wave that impinges on the same structure [Fig. 4(e)] is longitudinal instead of transverse, it is strongly reflected. By contrast, Figs. 4(i) and 4(j) show

that as the incidence direction is changed to the ΓM direction, longitudinal waves instead of transverse waves pass through the structure and preserve their plane-wave characteristic. All these cases show that the PC near the Dirac point frequency can guide transverse (longitudinal) waves around an obstacle along the ΓX (ΓM) incidence direction. These simulation results can be expected from the effective medium description of the system and highlight the super-anisotropy as well as the effective zero index of the PC near the Dirac point. In addition, in Fig. 5, we also show that numerical simulations (with the COMSOL MULTIPHYSICS) of such effects can be observed in a homogenous anisotropic medium. All the effective medium parameters (ρ_{eff}, C_{11}^{eff}, C_{12}^{eff}, and C_{44}^{eff}) can be obtained from Fig. 3 at the frequency above the Dirac point frequency. We also note that such effects, sometimes referred to as cloaking effects, are well established for electromagnetic wave zero-refractive index materials,[41] but the physics is more complex here due to the super-anisotropic effect.

IV. SUMMARY

In summary, 2D elastic wave crystals consisting of a square lattice of cylinders can be designed to exhibit Dirac cone dispersion at $\vec{k}=0$ by exploiting dipolar and quadrupolar accidental degeneracy. They are very unusual systems in which the Dirac cone modes have equifrequency contours that are almost circular (i.e. the system appears to be isotropic), but the eigenmodes are super-anisotropic as only transverse modes are allowed to propagate along the ΓX direction, while only longitudinal modes along the ΓM direction. Such solid-like in one direction and liquid-like in other direction[42] propagation properties cannot be found in electromagnetic or acoustic counterparts with Dirac cone at $\vec{k}=0$. Furthermore, we showed that such PCs behave like elastic wave materials with an effectively zero refractive index.

ACKNOWLEDGMENTS

*phchan@ust.hk

[1] R. A. Sepkhanov, Y. B. Bazaliy, and C. W. J. Beenakker, Phys. Rev. A **75**, 063813 (2007).

[2] Y. D. Chong, X. G. Wen, and M. Soljacic, Phys. Rev. B **77**, 235125 (2008).

[3] F. D. M. Haldane and S. Raghu, Phys. Rev. Lett. **100**, 013904 (2008).

[4] S. Raghu and F. D. M. Haldane, Phys. Rev. A **78**, 033834 (2008).

[5] X. Zhang, Phys. Rev. Lett. **100**, 113903 (2008).

[6] X. Zhang and Z. Liu, Phys. Rev. Lett. **101**, 264303 (2008).

[7] T. Ochiai and M. Onoda, Phys. Rev. B **80**, 155103 (2009).

[8] D. Han, Y. Lai, J. Zi, Z. Q. Zhang, and C. T. Chan, Phys. Rev. Lett. **102**, 123904 (2009).

[9] T. Ochiai, J. Phys. Condens. Matter **22**, 225502 (2010).

[10] Xueqin Huang, Yun Lai, Zhi Hong Hang, Huihuo Zheng, and C. T. Chan, Nat. Mater. **10**, 582 (2011).

[11] R. W. Ziolkowski, Phys. Rev. E **70**, 046608 (2004).

[12] A. Alu, M. G. Silveirinha, A. Salandrino, and N. Engheta, Phys. Rev. B **75**, 155410 (2007).

[13] M. G. Silveirinha and N. Engheta, Phys. Rev. Lett. **97**, 157403 (2006).

[14] R. Liu, Q. Cheng, T. Hand, J. J. Mock, T. J. Cui, S. A. Cummer, and D. R. Smith, Phys. Rev. Lett. **100**, 023903 (2008).

[15] B. Edwards, A. Alu, M. E. Young, M. Silveirinha, and N. Engheta, Phys. Rev. Lett. **100**, 033903 (2008).

[16] J. Hao, W. Yan, and M. Qiu, Appl. Phys. Lett. **96**, 101109 (2010).

[17] V. C. Nguyen, L. Chen, and K. Halterman, Phys. Rev. Lett. **105**, 233908 (2010).

[18] Zhengyou Liu, Xixiang Zhang, Yiwei Mao, Y. Y. Zhu, Zhiyu Yang, C. T. Chan, and Ping Sheng, Science **289**, 1734 (2000).

[19] J. Li and C. T. Chan, Phys. Rev. E **70**, 055602(R) (2004).

[20] Nicholas Fang, Dongjuan Xi, Jianyi Xu, Muralidhar Ambati, Werayut Srituravanich, Cheng Sun, and Xiang Zhang, Nature Mater. **5**, 452 (2006).

[21] G. W. Milton, M. Briane and J. R. Willis, New J. Phys. **8**, 248 (2006).

[22] Y. Ding, Z. Liu, C. Qiu, and J. Shi, Phys. Rev. Lett. **99**, 093904 (2007).

[23] Y. Wu, Y. Lai, and Z. Q. Zhang, Phys. Rev. B **76**, 205313 (2007).

[24] D. Torrent and J. Sanchez-Dehesa, New J. Phys. **10**, 023004 (2008).

[25] D. Torrent and J. Sanchez-Dehesa, New J. Phys. **10**, 063015 (2008).

[26] S. A. Cummer, B. I. Popa, D. Schurig, D. R. Smith, J. Pendry, M. Rahm, and A. Starr, Phys. Rev. Lett. **100**, 024301 (2008).

[27] A. N. Norris, Proc. R. Soc. A **464**, 2411 (2008).

[28] M. Farhat, S. Guenneau, and S. Enoch, Phys. Rev. Lett. **103**, 024301 (2009).

[29] S. H. Lee, C. M. Park, Y. M. Seo, Z. G. Wang, and C. K. Kim, Phys. Rev. Lett. **104**, 054301 (2010).

[30] S. Zhang, C. Xia, and N. Fang, Phys. Rev. Lett. **106**, 024301 (2011).

[31] X. Zhu, B. Liang, W. Kan, X. Zou, and J. Cheng, Phys. Rev. Lett. **106**, 014301 (2011).

[32] Q. Ni and J. Cheng, Phys. Rev. B **72**, 014305 (2005).

[33] Y. Wu and Z. Q. Zhang, Phys. Rev. B **79**, 195111 (2009).

[34] Yun Lai, Ying Wu, Ping Sheng, and Zhao-Qing Zhang, Nature Mater. **10**, 620 (2011).

[35] D. Royer and E. Dieulesaint, *Elastic Waves in Solids I* (Springer, New York, 1999), p. 177.

[36] L. D. Landau and E. M. Lifshitz, *Theory of Elasticity* (Butterworth-Heinemann, Oxford, 1986), p. 92.

[37] M. S. Kushwaha, P. Halevi, G. Martínez, L. Dobrzynski, and B. Djafari-Rouhani, Phys. Rev. B **49**, 2313 (1994).

[38] J. O. Vasseur, P. A. Deymier, B. Chenni, B. Djafari-Rouhani, L. Dobrzynski, and D. Prevost, Phys. Rev. Lett. **86**, 3012 (2001).

[39] R. V. Craster, J. Kaplunov, and A. V. Pichugin, Proc. R. Soc. London A **466**, 2341 (2010).

[40] R. V. Craster, J. Kaplunov, E. Nolde, and S. Guenneau, J. Optical Society America A **28**, 1032 (2011).

[41] See, for example, J. Hao, W. Yan, and M. Qiu, Appl. Phys. Lett. **96**, 101109 (2010).

[42] J. Page, Nat. Mater. **10**, 565 (2011).